A linear stability approach to vortex-induced vibrations and waves

R. Violette[a,b], E. de Langre[a,*], J. Szydlowski[b]

[a]*Department of Mechanics, LadHyX, CNRS-Ecole Polytechnique, 91128 Palaiseau, France*
[b]*Institut Français du Pétrole, 1-4 av. de Bois Préau, 92852 Rueil-Malmaison, France*

Abstract

The motion induced by vortex shedding on slender flexible structures subjected to cross-flow is considered here. This phenomenon of vortex-induced vibration (VIV) is analysed by considering the linear stability of a coupled system that includes the structure dynamics and the wake dynamics. The latter is modelled by a continuum of wake oscillators, distributed along the span of the structure. In the case of uniform flows over a straight tensioned cable, VIV are found to arise as an instability related to the merging of two waves. In the case of a cable of finite length, the selection of modes that experience lock-in with the wake is found using the same stability argument. In non-uniform flows, several unstable wave systems are identified, and competition between them is discussed. Comparison is then made with existing experimental and computational data of VIV of slender structures under uniform and non-uniform flows. Phenomena previously identified in these systems, such as mode switching when the flow velocity is varied, time sharing of the response between two frequencies, or the coexistence of several regions of VIV with different dynamics in the same structure, are discussed with the help of the proposed model.
© 2010 Elsevier Ltd. All rights reserved.

Keywords: Vortex-induced vibrations; Linear stability; Wake-oscillator model; Flexible structures; Waves

1. Introduction

Vortex induced vibrations (VIV) of cylindrical structures has been the subject of extensive theoretical, experimental and numerical studies, see for instance Williamson and Govardhan (2004), Sarpkaya (2004) and Gabbai and Benaroya (2005) for recent reviews. A bluff body undergoing VIV can reach an amplitude of motion in the direction transverse to the flow of the order of one diameter. This occurs when the period of vortex shedding is comparable to the free oscillation period of the structure. A strong interaction then takes place between the cylinder and its wake, and both elements oscillate at the same frequency, hence the term lock-in. The underlying impacts of this phenomenon on engineering applications, such as undesirable vibrations of offshore structures, chimneys and heat exchanger tubes, explain the deep interest in the subject. In fact, sustained vibrations of those structures can lead to failures by fatigue or unacceptable increases of the drag on the system.

---

*Corresponding author.
E-mail address: delangre@ladhyx.polytechnique.fr (E. de Langre).

Nomenclature

A	couping parameter
B	bending stiffness
C_D	drag coefficient
C_{L_0}	lift coefficient
C_{M_0}	added mass coefficient
D	cable diameter
F_Y	fluid loading on the cable
G	ratio between wake and cable amplitude
j	number of discretization points for the wake variable
$k, \overline{k}$	dimensionless wavenumber, normalized wavenumber
L	length of cable
m_S	mass per unit length of the structure
m_T	mass per unit length, including added mass
m^*	mass ratio
M	mass number
$N_{1,2}$	amplitude of waves propagating toward negative z
$p, \overline{p}$	dimensionless wavenumber, normalized wavenumber
$P_{1,2}$	amplitude of waves propagating toward positive z
q	wake variable
$\hat{q}$	complex amplitude of the wake part of a wave
r	number of discretization points for the cable variable
R	velocity ratio
s	structural wave
S_T	Strouhal number
$t, \overline{t}, T$	dimensionless time, normalized time, time

u	reduced flow velocity
U	flow velocity
v	dimensionless flow velocity
V_y, V_q	eigenvectors for the structure and the wake
w	wake wave
y, Y	dimensionless cable cross-flow displacement, cable cross-flow displacement
$\hat{y}$	complex amplitude of the cable part of a wave
Y_N	modal weight according to Chaplin et al. (2005b)
z, Z	dimensionless spanwize coordinate, spanwise coordinate
$\mathcal{B}$	wave velocity in a cable with bending stiffness
$\mathcal{C}$	wave velocity in a tensioned cable
$\mathcal{D}$	dispersion relation between frequency and wavenumber
$\mathcal{K}$	stiffness matrix
$\mathcal{M}$	mass matrix
$\mathcal{Q}$	discretized form of the wake variable
$\mathcal{R}$	damping matrix
$\mathcal{Y}$	discretized form of the cable variable
γ	fluid added damping coefficient
Γ	dimensionless bending stiffness
ε	growth rate parameter of the wake oscillator
ζ_S	damping
θ	tension profile
Θ	maximum tension along the cable
μ	mass parameter
ρ	fluid density
Ψ	spanwise variation of the flow velocity
$\omega, \overline{\omega}$	dimensionless frequency, normalized frequency

In this paper, the focus is on slender structures undergoing VIV, the engineering application being related to offshore systems such as mooring cables or underwater piping elements called risers. Those practical cases are characterized by a flexible bluff body having an aspect ratio, length over diameter, of order 10^3 and a ratio of structural mass over fluid displaced mass of the order of one. As reported from field studies (Alexander, 1981; Kim et al., 1985; Vandiver, 1993; Marcollo et al., 2007), the vortex-induced motion of those structures is sometimes characterized by travelling waves. Since the ocean or sea currents usually vary with depth, those structural waves may develop in non-uniform flow conditions.

Considerable knowledge has been gained on the physics of the interaction between a rigid cylinder and its wake when the former is undergoing a prescribed motion [for example Sarpkaya (1978), Gopalkrishnan (1993), Carberry et al. (2005)] or is free to move transverse to the flow direction when supported elastically [for example Khalak and Williamson (1999), Vikestad et al. (2000)].

The behaviour of high aspect ratio flexible structures under non-uniform or even uniform flows is, however, much less understood. Even though there are similarities between the phenomenology of VIV of rigid and flexible bodies as reported by Brika and Laneville (1993) and Fujarra et al. (2001), there is indeed a gap between the two situations. Several aspects must be taken into account: (a) in very slender structures the number of vibration modes that may interact with the wake is large, (b) the local wake depends on the local cross-flow that may vary in intensity and direction along the structure, (c) in practical applications boundary conditions at the extremities of the structure may be quite dissipative, and a wave description may be more appropriate than a mode description. This leads to questions that are definitely more complex than in the case of an elastically supported rigid cylinder under uniform flows, as often used

in analytical studies. For example, the issue of the range of flow velocities that may lead to lock-in differs: for an elastically supported rigid cylinder this is well defined, see for example King et al. (1973) and Griffin and Ramberg (1982), and may easily related to the ratio of the frequency of shedding and that of the cylinder, with some effect of mass ratio and structural damping. When the number of modes that may lock-in is large, several time scales are present in the problem, and the existence of one or several simultaneous lock-in must be evaluated. Moreover, as the oncoming flow may vary in space, several time scales of vortex shedding may also exist, further complicating the problem. Finally, the possibility of travelling waves exists.

In fact, there are a number of publications reporting laboratory experiments on VIV of high aspect ratio structures that bring some answers to the questions above, for example King (1995), Chaplin et al. (2005b), Trim et al. (2005), and Lie and Kaasen (2006). In King (1995), results are reported from a tensioned cable under uniform water flow. As the flow velocity is increased, the frequency of motion increases by steps. Each step corresponds to the lock-in range of a distinct structural mode. This type of experimental result was also reported more recently by Chaplin et al. (2005b). Conversely, Trim et al. (2005), when testing a high aspect ratio tensioned beam in uniform flows, observed that the evolution of motion frequency is rather continuous with velocity.

In Chaplin et al. (2005b), it is also reported that VIV in uniform flows can be either highly periodic or, in some cases, strongly modulated with time in terms of modal content of the response. In the latter case, the response would "switch" from one dominant spatial mode to another, justifying the name "mode switching" used by Chaplin et al. (2005b) for this phenomenon. The same behaviour was also observed from field experiments with a very high aspect ratio riser in non-uniform currents, where distinct frequencies of movement were "sharing" time (Swithenbank, 2007) leading to the term of "time sharing" which we shall use here.

Numerical computations of VIV of slender structures are also available in the literature, where the Navier–Stokes equations and the structural equations are solved jointly (Newman and Karniadakis, 1997; Lucor et al., 2006). Due to the extensive computational cost, there are few three-dimensional computations for high aspect ratio systems. Newman and Karniadakis (1997) found a cable response in form of a travelling wave in uniform flows, but they obtained a mixture of standing and travelling waves for a non-uniform flow. Lucor et al. (2006) studied a very high aspect ratio tensioned beam with non-uniform flow loading. They reported that the structure vibration frequencies varied with space, the low frequencies being located at low flow velocity region and the high frequencies at the high flow velocity region. This spatial variation of dominant vibration frequencies in non-uniform flows is also observed experimentally (Kim et al., 1985).

Apart from numerical solutions of the Navier–Stokes equations, one can rely on semi-empirical models for predictions. By semi-empirical, it is meant that results from rigid cylinder experiments are used as inputs to predict VIV of slender flexible structures. These models can be divided into two subgroups. For the first subgroup, the hydrodynamic loading on the structure is function of its own movement. For example, Sarpkaya (1978) decomposes this loading into two components: one in phase with the acceleration and the other with velocity. The dependency of those quantities on the movement of the structure is then obtained experimentally [see for example Gopalkrishnan (1993)]. This approach is widely used in industry, see Vandiver (1994). On the other hand, from experimental observations of the time evolution of the lift force due to vortex shedding, Birkoff and Zarantanello (1957) and Bishop and Hassan (1964) suggested that this quantity could be regarded as resulting from the dynamics of an oscillator. This is the basic idea of the second subgroup of the semi-empirical models, where the wake dynamics is modelled by a nonlinear oscillator, leading to the term "wake oscillator models". Since the development of the first wake oscillator model by Hartlen and Currie (1970), several models have been introduced with different nonlinearities for the wake equation and different coupling functions between the wake and the structure. In a recent paper, Gabbai and Benaroya (2008) have shown that a number of wake oscillator models in the literature can be recovered from using Hamilton's principle, proving, to some degree, that this family of models has some relevance in terms of fluid dynamics. More generally, representing the dynamics of the wake by a single self-sustained nonlinear oscillator is consistent with the idea of a nonlinear global mode which is characterized by its frequency, growth rate, and amplitude (Chomaz, 2005). Using a van der Pol oscillator to model the fluctuating lift, Facchinetti et al. (2004a) showed that the most appropriate forcing on the wake variable for reproducing the physics of lock-in was proportional to the acceleration of the structure. Using distributed wake oscillators along the span of the structure, the model was then extended to flexible structures subjected to uniform and non-uniform flows (Facchinetti et al., 2004b; Mathelin and de Langre, 2005) and validated against results from numerical simulations and experiments on high aspect ratio flexible structures under non-uniform flows (Violette et al., 2007). This model has also been used by other authors since then to study certain aspects of VIV of slender structures in non-uniform flows (Mukundan et al., 2009; Xu et al., 2008).

In Chaplin et al. (2005a), comparisons for a tensioned beam in uniform flows between experimental results and most existing prediction methods are presented. Those methods succeed at different levels at predicting quantitatively the experimental results. However, there is certainly a need for a systematic and comprehensive approach to address the

issues raised above, that are specific to slender structures: simultaneous lock-in of several modes, travelling waves, time sharing and separation in space of dominant frequencies. The focus needs to be more on the mechanisms that lead to such behaviours than on the quantitative prediction.

In a recent paper, de Langre (2006) modelled vortex-induced vibrations of an elastically supported rigid cylinder under uniform flow using a linearized version of Facchinetti's wake oscillator model. He showed that the lock-in mechanism between the wake and the structure can be modelled as a linear instability arising from the merging of the frequencies of the two modes of the system: namely a structure-dominated mode and a wake mode. This type of instability is commonly called coupled-mode flutter (Blevins, 1990). Using this simple approach, de Langre retrieved analytically the influence of the different parameters on the characteristics of lock-in. Clearly, such a linear stability approach could not lead to estimations of the amplitude of the steady-state motion of the cylinder. Still, it was found that some characteristics of the steady-state regime, such as the frequency or the dependence on mass ratio, did not differ much from those of the most unstable mode found in the linear stability approach. More generally, this allows one to describe the lock-in between a flow instability and a vibration mode of a structure in a linear framework: see for instance the case of flow over a canopy (Py et al., 2006; Gosselin and de Langre, 2009), where a mixing layer instability interacts with a flexible system.

Following the approach of de Langre (2006), the purpose of this paper is therefore to present a simple theory for vortex-induced vibrations of slender flexible structures based on a linear stability analysis, and thereby to furnish simple explanations to the questions raised in this introduction. In Section 2, we present the linear wake oscillator stability theory used for comparisons with experiments and numerical results reported in the literature.

2. A linear wake oscillator model for Vortex-Induced Vibrations under uniform flow

2.1. Model description

For the vibrating structure, a tensioned cable model is considered here for simplicity. Considering only the cross-flow movement of the cable, its equation of motion in dimensional form is

$$m_S \frac{\partial^2 Y}{\partial T^2} + \zeta_S \frac{\partial Y}{\partial T} - \Theta \frac{\partial^2 Y}{\partial Z^2} = F_Y, \tag{1}$$

$Y(Z,T)$ being the structure displacement at the spanwise position Z and time T, Θ being the tension, m_S the linear density of the cable and ζ_S the structural damping coefficient. Following Facchinetti et al. (2004b), the fluid force F_Y is written as

$$F_Y = \frac{1}{4}\rho U^2 D C_{L_0} q(Z,T) - \frac{\pi}{4}\rho D^2 C_{M_0}\frac{\partial^2 Y}{\partial T^2} - \frac{1}{2}\rho D C_D U \frac{\partial Y}{\partial T}, \tag{2}$$

where ρ is the fluid density, D the cross-sectional diameter, U the flow velocity, C_{M_0} the inviscid added mass coefficient, C_D the mean sectional drag coefficient and C_{L_0} the fluctuating lift coefficient amplitude for a rigid cylinder under uniform flow. The dynamics of the local fluctuating lift coefficient $q(Z,T) = 2C_L(Z,T)/C_{L_0}$ appearing in the forcing term F_Y is here modelled using a linear oscillator, following de Langre (2006):

$$\frac{\partial^2 q}{\partial T^2} - \varepsilon\left(2\pi S_T \frac{U}{D}\right)\frac{\partial q}{\partial T} + \left(2\pi S_T \frac{U}{D}\right)^2 q = A\frac{\partial^2 Y}{\partial T^2}, \tag{3}$$

where S_T is the Strouhal number. The forcing of the structure over the wake is proportional to its local cross-flow acceleration through an empirical constant A, see Facchinetti et al. (2004b). In this simple model, the phenomenology must be introduced through the coefficients C_{L_0}, C_D, S_T, A and ε. Of these, the first three quantities are well documented, for instance in terms of their dependency on the Reynolds number (Norberg, 2003). The empirical parameters $\varepsilon = 0.3$ and $A = 12$ are deduced from wake measurements obtained from forced vibration experiments on rigid cylinders (Facchinetti et al., 2004a). Note that no spanwise interaction of the wake variable q is considered: an interaction by diffusing and stiffening terms was studied by Mathelin and de Langre (2005) for flexible structures and it was shown then that its effect was negligible, the spanwise interaction in the wake resulting essentially from the structure movement.

Eq. (3) apparently allows the wake variable, q, to be discontinuous in Z, because of the absence of space derivatives in Z. Yet, the coupling with the structural variable, Y, which is continuous in Z, Eq. (1), prevents any discontinuity. Physically this means that the correlation in Z in the wake is actually driven by the correlation in the motion of waves in the cable, which is much stronger than spanwise fluid effects. See also Facchinetti et al. (2002) for a case where the
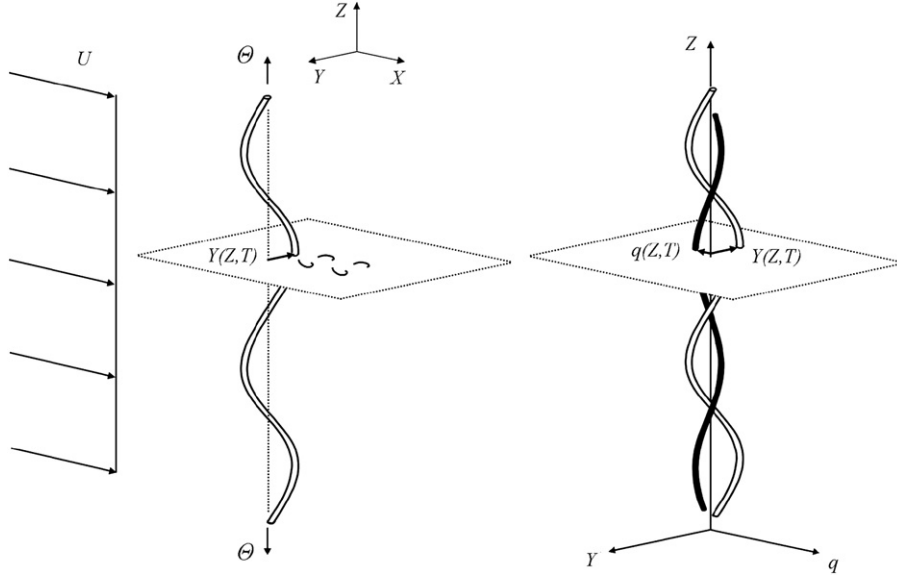
Fig. 1. Model of a tensioned structure undergoing vortex-induced vibrations VIV. Left: transverse displacement Y and tension Θ. Right: schematic view of the model using a distributed wake oscillator variable q.

cable is fixed and fluid spanwise coupling is needed to recover the shedding dynamics in sheared flow, and Violette et al. (2007) for comparison between a nonlinear wake oscillator model with no spanwise correlation and DNS results.

From Eqs. (1) and (3), the wake and the structure will now be considered as a single one-dimensional medium, the dynamics of which is defined by $Y(Z,T)$ and $q(Z,T)$. This medium will be analysed with propagating wave solutions. These propagating waves have two components, namely the structure displacement $Y(Z,T)$ and the lift fluctuation $q(Z,T)$, Fig. 1.

2.2. Dimensionless form

Eqs. (1) and (3) are now put in dimensionless form. The cable undamped phase velocity in stagnant fluid $\mathcal{C}$ is used to define the dimensionless time

$$\mathcal{C} = \sqrt{\frac{\Theta}{m_T}}, \tag{4}$$

where $m_T = m_S + (\pi/4)\rho D^2 C_{M_0}$ is the sum of the structure mass and the inviscid fluid added mass. Using the diameter D as the reference length scale, the dimensionless time t, displacement y and spanwise position z are expressed respectively as $t = \mathcal{C}T/D$, $y = Y/D$ and $z = Z/D$. The dimensionless equations are then

$$\frac{\partial^2 y}{\partial t^2} + \left(\xi + \frac{\gamma}{\mu} u \right) \frac{\partial y}{\partial t} - \frac{\partial^2 y}{\partial z^2} = M u^2 q, \tag{5}$$

$$\frac{\partial^2 q}{\partial t^2} - \varepsilon u \frac{\partial q}{\partial t} + u^2 q = A \frac{\partial^2 y}{\partial t^2}, \tag{6}$$

where

$$\xi = \left(\frac{D}{m_T \mathcal{C}} \right) \zeta_S, \quad \gamma = \frac{C_D}{4\pi S_T}, \quad M = \frac{C_{L_0}}{16\pi^2 S_T^2 \mu}, \quad \mu = \frac{m_T}{\rho D^2}. \tag{7}$$

As outlined by Facchinetti et al. (2004a), M is a mass number that scales the effect of the wake on the structure, and μ is a mass parameter, related to the often-used mass ratio m^* by $m^* = (4\mu/\pi) - C_{M_0}$.

The parameter u is referred to as the reduced velocity and is defined by

$$u = 2\pi S_T \frac{U}{C}. \tag{8}$$

Note that this definition of the reduced velocity differs from the more usual $U_R = U/fD$ in VIV of discrete systems. Here the flow velocity U is referred to C, the velocity of waves in the tensioned cable.

In de Langre (2006), it was shown that damping terms did not significantly affect the instability mechanism causing lock-in, although they do modify the value of velocity where the instability arises. We therefore disregard them now for the sake of simplicity, but will re-introduce them when comparing with experiments. The set of equations used in the theoretical development in the next two sections therefore simply read

$$\frac{\partial^2 y}{\partial t^2} - \frac{\partial^2 y}{\partial z^2} = Mu^2 q, \tag{9}$$

$$\frac{\partial^2 q}{\partial t^2} + u^2 q = A\frac{\partial^2 y}{\partial t^2}. \tag{10}$$

Only three dimensionless parameters, u, A and M are left in this model of vortex-induced motion of a tensioned cable. The control parameter is u, the reduced velocity, which scales the flow velocity with the velocity of waves in the cable, Eq. (8). The parameter A scales the sensitivity of the wake dynamics to the motion of the cylinder, Eq. (3), while M is essentially a mass number, Eq. (7). Their respective values are of the order of 10 for A ($A = 12$ was found by Facchinetti et al.), and 10^{-2} for M in the case of neutrally buoyant structures, such as found in offshore engineering. These two parameters only affect the result through their product AM, as can be seen by a change of variable using q/A. The typical order of magnitude of the combined parameter AM is therefore 10^{-1}. We will refer to the AM term as the *combined mass number*, in reference to its dependency on the mass number M.

3. Linear stability analysis in the case of uniform flow

3.1. Infinite tensioned cable

The stability analysis of the system (9) and (10) is presented first for the case of an infinite cable-wake medium. Searching for solutions in the form of propagating waves

$$\begin{bmatrix} y(z,t) \\ q(z,t) \end{bmatrix} = \begin{bmatrix} \hat{y} \\ \hat{q} \end{bmatrix} e^{i(\omega t + kz)}, \tag{11}$$

where ω is the frequency, k the wavenumber, $\hat{y}$ and $\hat{q}$ the complex amplitude of the structural and wake part of the waves respectively, the dispersion relation reads

$$\mathcal{D}(\omega, k; u) = \omega^4 + [(AM-1)u^2 - k^2]\omega^2 + k^2 u^2 = 0. \tag{12}$$

Note that this relation can be put in the reduced form $\overline{\mathcal{D}}(\omega/u, k/u) = 0$; however, the form (12) is kept in order to facilitate the physical interpretation of the results. The stability analysis of the cable-wake is now done for the temporal problem, i.e. with k real. The pulsation ω as a function of k and u is derived from (12),

$$\omega(k,u) = \pm \frac{1}{\sqrt{2}} \left[k^2 + (1-AM)u^2 \pm \sqrt{(k^2 + (1-AM)u^2)^2 - 4k^2 u^2} \right]^{1/2}. \tag{13}$$

Frequencies come in pairs of opposite sign corresponding to propagation in opposite directions. Assuming $AM < 1$, which is consistent with practical cases, ω is complex when

$$-2ku < k^2 + (1-AM)u^2 < 2ku. \tag{14}$$

The range of wavenumbers k that give complex ω at a given reduced velocity u is therefore

$$u(1-\sqrt{AM}) < k < u(1 + \sqrt{AM}). \tag{15}$$

For wavenumbers that satisfy (15), the complex frequency is

$$\omega_{\pm} = \frac{1}{2}\sqrt{k^2 + 2uk + (1-AM)u^2} \pm \frac{i}{2}\sqrt{-k^2 + 2uk + (AM-1)u^2}. \tag{16}$$

From Eq. (16), two unstable and two damped waves are found for each wavenumber inside the range defined by (15). This defines a temporal instability for the coupled cable-wake system.

Before going any further, the physical characteristics of this instability are analysed. Fig. 2 illustrates the real and imaginary part of ω as a function of k for typical values of AM. Here, the velocity u is taken equal to one, recalling that the dispersion relation may be put in a reduced form on ω/u and k/u. The figure also shows the ratio G between the wake amplitude and the cable amplitude

$$G = \frac{\hat{q}}{\hat{y}} = \frac{k^2 - \omega^2}{Mu^2} = \frac{A\omega^2}{\omega^2 - u^2}. \tag{17}$$

These results may be interpreted as follows. For wavenumbers outside the lock-in range defined by relation (15), two waves are found: one with a strong wake amplitude (denoted w) and one with a strong structure amplitude (denoted s). The frequency of the s waves increases linearly with k, which is expected for a tensioned cable. The frequency is nearly constant for the w waves, which is expected for a wake with no spanwise interaction. The two wave frequencies merge in the lock-in range leading to complex conjugates frequencies ω. This is identified on the figure as coupled-wave flutter (cwf). In this range of wavenumbers the phase angle between the cable and the wake varies from π to 2π.

From Fig. 2, it is found that the cable-wake medium displays a temporal instability, similar to that of the elastically supported rigid cylinder reported by de Langre (2006). It results from the merging of the frequencies of two neutral waves, a structural wave s and a wake wave w. For a given reduced velocity u, the most unstable wavenumber is
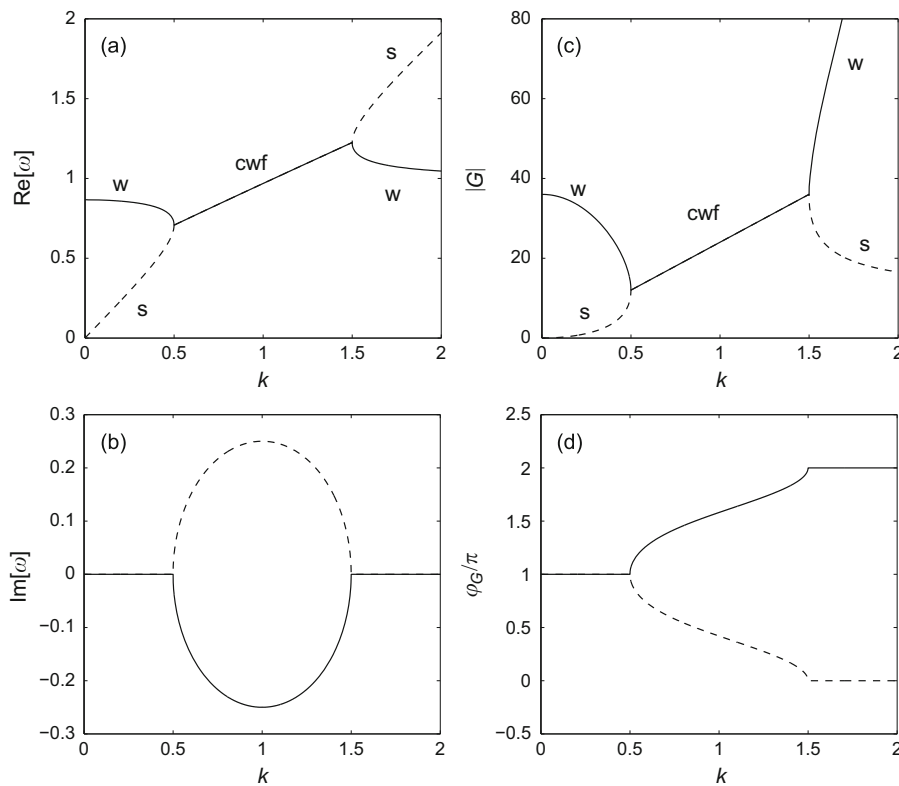

Fig. 2. Linear stability analysis of vortex-induced waves in the coupled wake-cable system. Temporal analysis, k real. The complex pulsation ω and the amplitude ratio G are shown as a function of the wavenumber k for a combined mass number $AM = 0.25$. The flow velocity is arbitrarily set to $u = 1$. (a) Real part of ω, (b) imaginary part of ω, (c) modulus of amplitude ratio $|G|$, (d) phase angle between the wake and the structure, φ_G. In the figure, "w" stands for a wake dominated wave, "s" for a structure dominated wave and "cwf" for the unstable wave resulting from coupled-wave flutter.

$k_{max} = u$. The corresponding complex pulsation reads

$$\omega_{max} = u\sqrt{1 - \frac{AM}{4}} - iu\frac{\sqrt{AM}}{2}. \tag{18}$$

Conversely, at a given wavenumber k, one can retrieve from Eq. (15), the range of reduced velocities u for which ω is complex

$$\frac{k}{1 + \sqrt{AM}} < u < \frac{k}{1 - \sqrt{AM}}. \tag{19}$$

The frequency ω is then given by Eqs. (16). Outside this range, Eq. (13) gives the neutral frequency. Fig. 3 shows the evolution of ω and G as a function of u for a given wavenumber. The same instability related to merging of the frequencies of two waves is observed. The evolutions of the pulsations and of the phase angle with the flow velocity are identical to that given in de Langre (2006) for an elastically supported rigid cylinder. This is expected, as fixing the wavenumber k is equivalent to replacing the spanwise second derivative of the displacement in (9) by a constant times the displacement: the equation for the structure is then identical to that of an elastically supported rigid cylinder.

3.2. Tensioned cable of finite length

We seek now to analyse the stability of the cable-wake medium when boundary conditions are imposed. This is done by imposing a restriction on the admissible wavenumbers. For a tensioned cable of dimensionless length $\Lambda = L/D$ with fixed ends, Fig. 4, the boundary conditions read

$$y(0, t) = 0, \quad y(\Lambda, t) = 0. \tag{20}$$

As no spanwise interaction is considered for the wake, no boundary condition is required on q. For a given complex frequency ω the wavenumbers given by the dispersion relation (12) come in pairs of opposite values, $k_1; k_2 = -k_1$. The
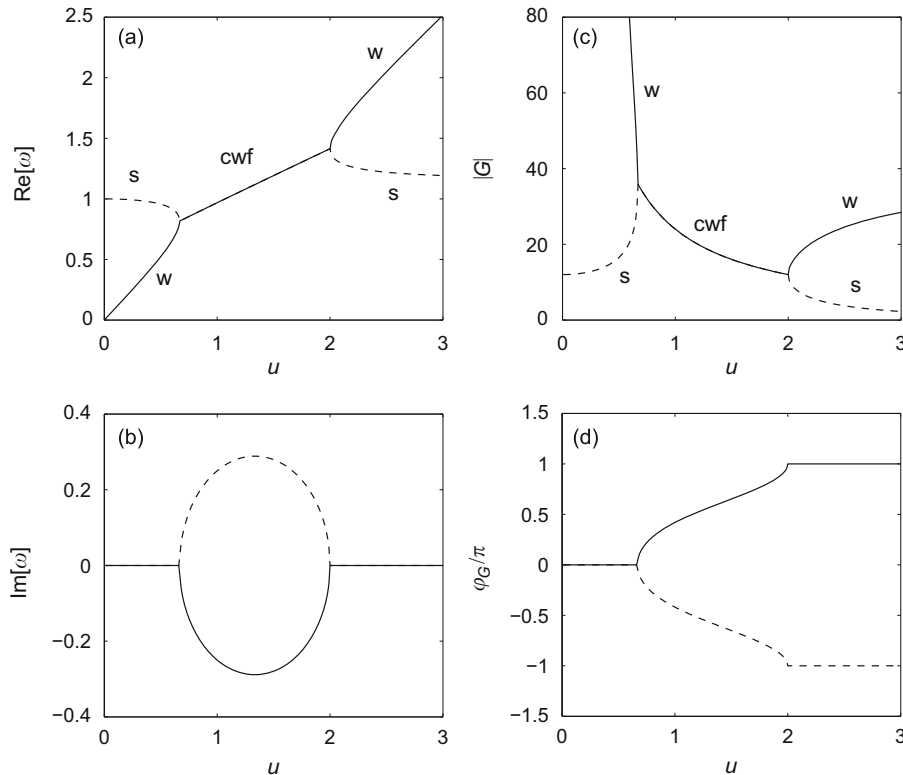

Fig. 3. Same results as Fig. 2, but as a function of the flow velocity u, for an arbitrary wave number $k = 1$. (a) Real part of ω, (b) imaginary part of ω, (c) modulus of $|G|$, (d) phase angle between the cable and the wake φ_G. Symbols s, w and cwf have same meaning as in Fig. 2.
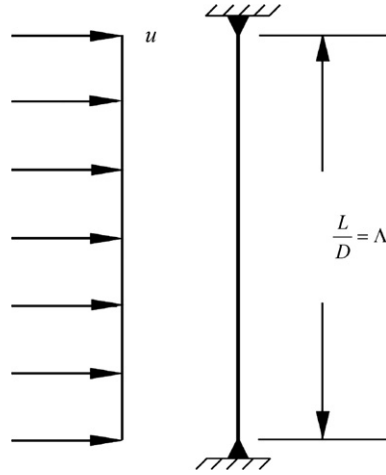
Fig. 4. Tensioned cable under a uniform flow. Extremities are fixed.

boundary condition (20) therefore implies that they are both real so that there is no exponential growth in space, even in this finite length case. Admissible real wavenumbers for such a configuration are thus

$$k_n = \frac{\pi}{\Lambda} n, \tag{21}$$

where $n = 1, 2, 3\ldots$. In this case, the terminology "mode number" applies to the variable n. Rewriting (19) using (21), one finds the range of reduced velocity in which Mode n is unstable

$$\left(\frac{\pi}{\Lambda}\right)\frac{n}{1+\sqrt{AM}} < u < \left(\frac{\pi}{\Lambda}\right)\frac{n}{1-\sqrt{AM}}. \tag{22}$$

Inside this range of reduced velocities, the frequency of Mode n is

$$\omega_n = \left(\frac{\pi}{2\Lambda}\right)[\sqrt{n^2 + 2n\beta + (1-AM)\beta^2} - i\sqrt{-n^2 + 2n\beta - (1-AM)\beta^2}], \tag{23}$$

with $\beta = u\Lambda/\pi$. Fig. 5 shows the evolution of ω with u for $n = 1, 2$ for two values of AM. For the sake of clarity, neutral frequencies are not shown. From Fig. 5, it is seen that $\mathrm{Re}[\omega]$ varies almost linearly with u and that the transition from one mode to another involves a jump in this quantity.

It can also be noticed that the range of instability for two adjacent modes can overlap. This is the case for $AM = 0.3$ but not for $AM = 0.05$. This shows that it is possible for more than one mode to be unstable for a given flow velocity. As seen in Fig. 5, the unstable modes have distinct frequencies. Using relation (22) and defining Δu_n as the range of reduced velocities where mode n and $n+1$ are both unstable, one finds

$$\Delta u_n = \frac{\pi}{\Lambda}\left[\left(\frac{2\sqrt{AM}}{1-AM}\right)n - 1\right]. \tag{24}$$

4. Linear stability analysis for non-uniform flow

Here, a generic case of non-uniform flow is studied. It consists of an infinite tensioned cable submitted to two uniform flow profiles, u_1 for $z > 0$ and u_2 for $z < 0$, with $u_1 > u_2$ (Fig. 6).

4.1. Configuration characteristics

Denoting ω_1, ω_2 and k, p the frequencies and wavenumber for Medium 1 and 2 respectively, the dispersion relations read

$$\mathcal{D}_1(\omega_1, k; u_1) = \omega_1^4 + [(AM-1)u_1^2 - k^2]\omega_1^2 + k^2 u_1^2 = 0, \tag{25}$$

$$\mathcal{D}_2(\omega_2, p; u_2) = \omega_2^4 + [(AM-1)u_2^2 - p^2]\omega_2^2 + p^2 u_2^2 = 0. \tag{26}$$
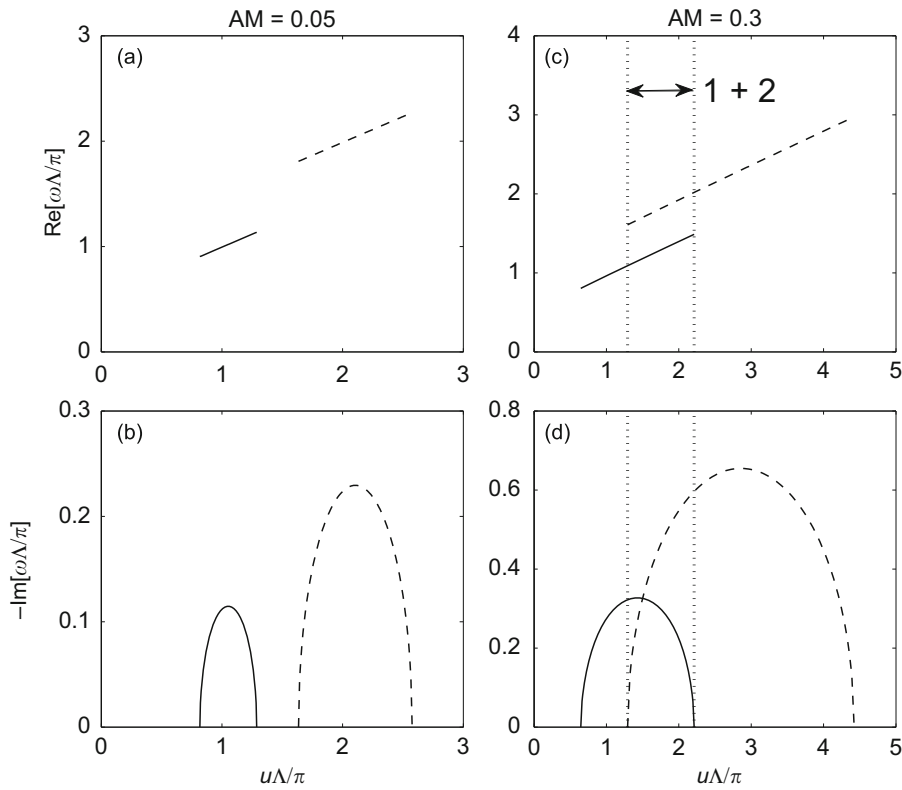
Fig. 5. Complex frequencies of the first two modes of the coupled wake-cable system for a cable of finite length, as a function of the flow velocity. Only unstable frequencies are shown. In the case $AM = 0.3$, right, a range exists where the two modes are simultaneously unstable. (a), (c) Evolution of Re[ω]; (b), (d) evolution of Im[ω]. Mode $n = 1$ (solid line), $n = 2$ (dashed line).
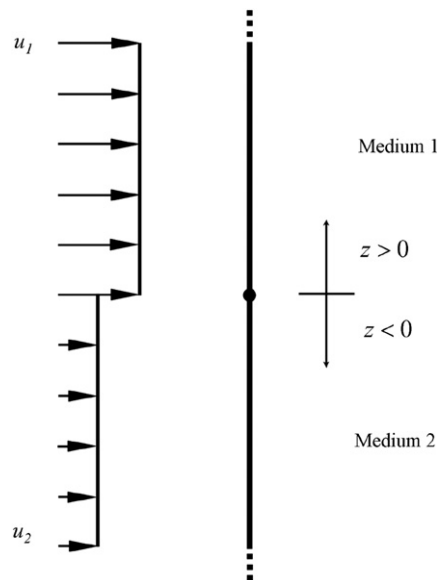

Fig. 6. Non-uniform flow on a straight cable. Two semi-infinite media having different reduced velocities u_1 and u_2 are connected at $z = 0$.

Solving Eqs. (25) and (26) for k and p one finds

$$k = \pm\omega_1\sqrt{1 + \frac{AMu_1^2}{\omega_1^2 - u_1^2}}, \quad p = \pm\omega_2\sqrt{1 + \frac{AMu_2^2}{\omega_2^2 - u_2^2}}. \tag{27}$$

The configuration shown in Fig. 6 implies a connection between the two media at $z = 0$. As no spanwise interaction is considered for the wake variable, this connection imposes conditions only on the structural part of the waves,

$$y_1(0, t) = y_2(0, t), \quad \frac{\partial y_1}{\partial z}(0, t) = \frac{\partial y_2}{\partial z}(0, t). \tag{28}$$

This implies that $\omega_1 = \omega_2 = \omega$. We restrict our analysis to temporally unstable wave systems, corresponding to a complex ω with a negative imaginary part. Also, only waves with finite amplitude at infinity are considered.

The cable displacement y and the fluctuating lift amplification q are included now in one variable for each medium, namely $\chi_1(z, t)$ and $\chi_2(z, t)$:

$$\begin{bmatrix} y_1(z, t) \\ q_1(z, t) \end{bmatrix} = \begin{bmatrix} 1 \\ \hat{q}_1/\hat{y}_1 \end{bmatrix} \chi_1(z, t), \quad \begin{bmatrix} y_2(z, t) \\ q_2(z, t) \end{bmatrix} = \begin{bmatrix} 1 \\ \hat{q}_2/\hat{y}_2 \end{bmatrix} \chi_2(z, t). \tag{29}$$

From Eq. (27) two waves are found in each medium. The response for the entire system is thus in the general form

$$\chi_1(z, t) = P_1 e^{i(\omega t + k^+ z)} + N_1 e^{i(\omega t + k^- z)}, \tag{30}$$

$$\chi_2(z, t) = P_2 e^{i(\omega t + p^+ z)} + N_2 e^{i(\omega t + p^- z)}, \tag{31}$$

where P and N are the amplitudes of the waves that are propagating toward positive and negative z respectively. For the sake of clarity, k and p are noted for now on without the $+$ and $-$ signs. Fig. 7 illustrates the type of response implied by Eqs. (30) and (31).
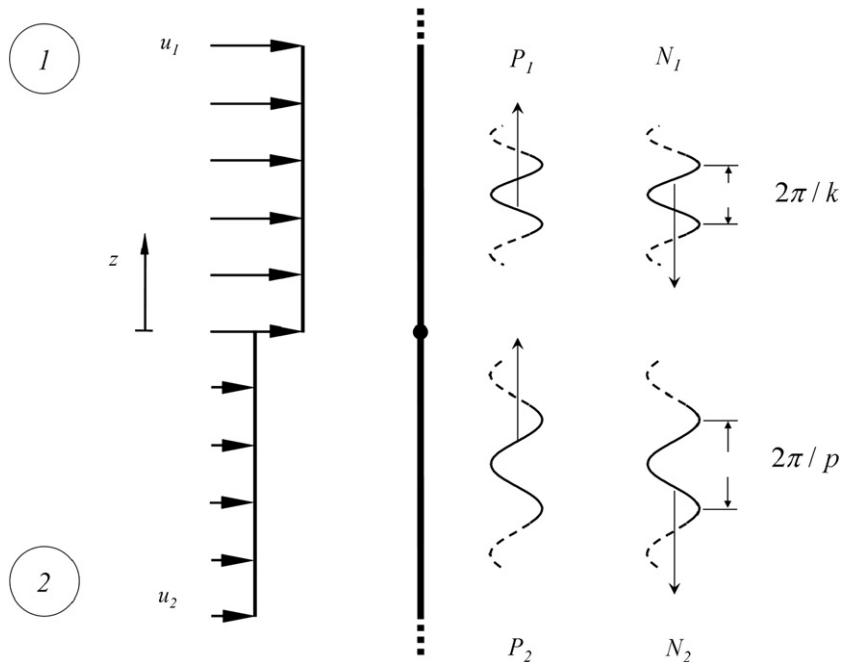

Fig. 7. Wave configuration corresponding to Eqs. (30) and (31).

4.2. Admissible wave systems

Admissible wave systems should satisfy (a) the dispersion relations (Eqs. (27)), (b) the connection condition (Eq. (28)) and (c) the condition of finite amplitude at infinity. The most general case implies complex values of k and p. From Eqs. (27), there is one wave in each medium that respects the finite amplitude condition at infinity, Fig. 8. However, condition (28) cannot be satisfied in this case if both wavenumbers are not equal. This form of response is thus not admissible.

The second type of response corresponds to both wavenumbers k and p being real. This configuration satisfies condition (28) for all wavenumbers. Since the complex frequency must be the same in both media, the ranges of unstable k and p must overlap. From Eq. (15) this condition reads

$$\frac{u_2}{u_1} \geq \frac{1-\sqrt{AM}}{\sqrt{1-AM}}. \tag{32}$$

This form of response is now referred to as the *conditional wave system* (C) because of this requirement, and is illustrated in Fig. 8.

The last possible type of response is composed of two neutral waves inside one medium and one wave with spatially decaying amplitude in the other medium. This form of response satisfies condition (28). Two new wave systems are thus identified: the first for which k is real and p is complex and the second with p real and k complex. The first wave system is from now on called the *primary wave system*, (P), and the second *secondary wave system*, (S), Fig. 8.

In order to compare wave systems, a common length scale is used to normalize the variables. This length scale is set equal to the most unstable wave length in Medium 1. From the discussion in Section 3.1, the corresponding wavenumber is $k_{max} = u_1$. The normalized quantities are therefore $\bar{z} = zu_1/2\pi$, $\bar{k} = k/u_1$ and $\bar{p} = p/u_1$. Variables t and ω are also normalized by u_1 in order to obtain $\bar{t} = tu_1/2\pi$ and $\bar{\omega} = \omega/u_1$. The velocity ratio $R = u_2/u_1$ is also introduced. The relations between the normalized variables $\bar{\omega}$, $\bar{k}$ and $\bar{p}$ read

$$\text{Re}[\bar{\omega}] = \frac{1}{2}\sqrt{\bar{k}^2 + 2\bar{k} + (1-AM)} = \frac{1}{2}\sqrt{\bar{p}^2 + 2R\bar{p} + (1-AM)R^2}, \tag{33}$$

$$\text{Im}[\bar{\omega}] = -\frac{1}{2}\sqrt{-\bar{k}^2 + 2\bar{k} + (AM-1)} = -\frac{1}{2}\sqrt{-\bar{p}^2 + 2R\bar{p} + (AM-1)R^2}, \tag{34}$$

$$\bar{k} = \pm\bar{\omega}\sqrt{1 + \frac{AM}{\bar{\omega}^2-1}}, \quad \bar{p} = \pm\bar{\omega}\sqrt{1 + \frac{AMR^2}{\bar{\omega}^2-R^2}}. \tag{35}$$
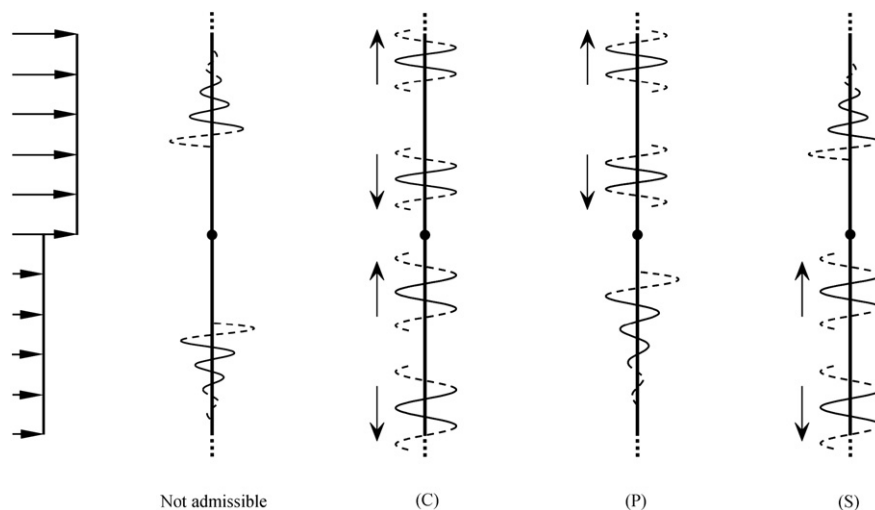

Fig. 8. Definition of the unstable wave systems in non-uniform flows: Left, two complex waves (nonadmissible); (C) four spatially neutral waves *conditional wave system*; (P) two spatially neutral waves and one spatially decaying, *primary wave system*; (S) two spatially neutral waves and one spatially decaying, *secondary wave system*.

At a given reduced velocity u, there is a real wavenumber for which the growth rate in time is maximum, see Section 3.1. The most unstable (P) wave system is for $\overline{k} = 1$. In the same way, the (S) system with the highest growth rate is for $\overline{p} = R$. The most unstable normalized frequency for each system thus reads, from Eq. (18),

$$\overline{\omega}_P = \sqrt{1 - \frac{AM}{4}} - i\frac{\sqrt{AM}}{2}, \quad \overline{\omega}_S = R\,\overline{\omega}_P. \tag{36}$$

Note that as $R < 1$, both the real and imaginary part of the complex frequency are smaller for (S) than (P).

While in (P) and (S) all frequencies are admissible, there is only one possible frequency $\overline{\omega}$ at a given velocity ratio R for the wave system (C). The corresponding wavenumbers are derived using (33) and (34)

$$\overline{k} = \pm R\sqrt{1 - AM}, \quad \overline{p} = \pm\sqrt{1 - AM}, \tag{37}$$

and the frequency reads

$$2\overline{\omega}_C = [2R\sqrt{\alpha} + \alpha(1 + R^2)]^{1/2} - i[2R\sqrt{\alpha} - \alpha(1 + R^2)]^{1/2}, \tag{38}$$

with $\alpha = 1 - AM$. It appears that the growth rate of the conditional wave system (C) is always smaller than that of both the (P) and (S) systems. We shall therefore assume that its role in the response can be neglected and will not discuss it any further.

4.3. Spatial forms of (P) and (S)

The spatial form of the wave systems (P) and (S) is examined here for fixed values of the velocity ratio R and of the combined mass number AM. A parametric analysis of their effect presented in Violette (2009), not shown here for the sake of brevity, shows that: (a) the form of the wave system is fairly independent on R and (b) high values of AM lead to stationary waves instead of propagating waves.

The evolution in space of wave systems (P) and (S) is fully determined by the wavenumbers $\overline{k}$ and $\overline{p}$ and the amplitude coefficients N_1, N_2, P_1 and P_2. For (P), we have $\overline{k} = 1$ and $\overline{p}$ is obtained from Eq. (35). The finite amplitude condition at infinity requires that $P_2 = 0$. The amplitudes N_1, N_2 and P_1 are determined from the connection conditions, Eq. (28). As there are only two equations for three unknowns, $N_1 = 1$ is used as a reference. Solving Eq. (28) for N_2 and P_2, one finds

$$[N_1, P_1, N_2, P_2] = [1, (1 - \overline{p})/(1 + \overline{p}), 2/(1 + \overline{p}), 0]. \tag{39}$$

Leaving out the growth in time of the amplitude, the response of (P) is shown in Fig. 9. The global response can be summarized as a wave propagating toward negative $\overline{z}$. Its amplitude decreases exponentially for $\overline{z} < 0$ and is spatially modulated for $\overline{z} > 0$. This modulation is caused by the relatively low modulus of P_1 with respect to the reference value N_1. Fig. 9 shows that there is a jump in amplitude for the wake variable at $\overline{z} = 0$, which is expected since the amplitude ratios $\hat{q}_1/\hat{y}_1$ and $\hat{q}_2/\hat{y}_2$ are not equal (Eq. (17)).

The spatial shape of (S) is found following the same steps. We have $\overline{p} = R$ and the wavenumber $\overline{k}$ is found with Eq. (35) for the pulsation obtained from Eq. (36). The amplitude coefficients read

$$[N_1, P_1, N_2, P_2] = [0, 2R/(R + \overline{k}), (R - \overline{k})/(R + \overline{k}), 1]. \tag{40}$$

Fig. 9 shows the form of the response (S). Except for the wavelength and the direction of propagation, the spatial form of (S) is similar to that of (P).

4.4. Coexistence of primary and secondary wave systems: space sharing

Considering that the growth rate of the wave system (P) is always larger than that of (S) one may expect that the former will dominate the long term steady-state response of the system. This is evidently true in Medium 1, the region of higher velocity, but not in Medium 2 where the amplitude of (P) exponentially decays with distance from the interface. Hence the question of how far into Medium 2 the wave system (P) penetrates must be analysed carefully, by taking into account both spatial and temporal forms. Still using the linear framework we consider the locus where both wave systems have the same amplitude, when an arbitrary unit initial condition is taken for both, Fig. 10(a). This locus moves into Medium 2 as time grows, as illustrated in Fig. 10(b). The phase velocity of this motion is given by

$$C_{PS} = \frac{\text{Im}[\overline{\omega}_P] - \text{Im}[\overline{\omega}_S]}{\text{Im}[\overline{p}_P]}. \tag{41}$$

This quantity is found to be of the order of unity, in dimensionless variables, and to depend on the velocity ratio R but weakly on the combined mass number AM, Fig. 10. This velocity scales the rate at which the wave system (P),
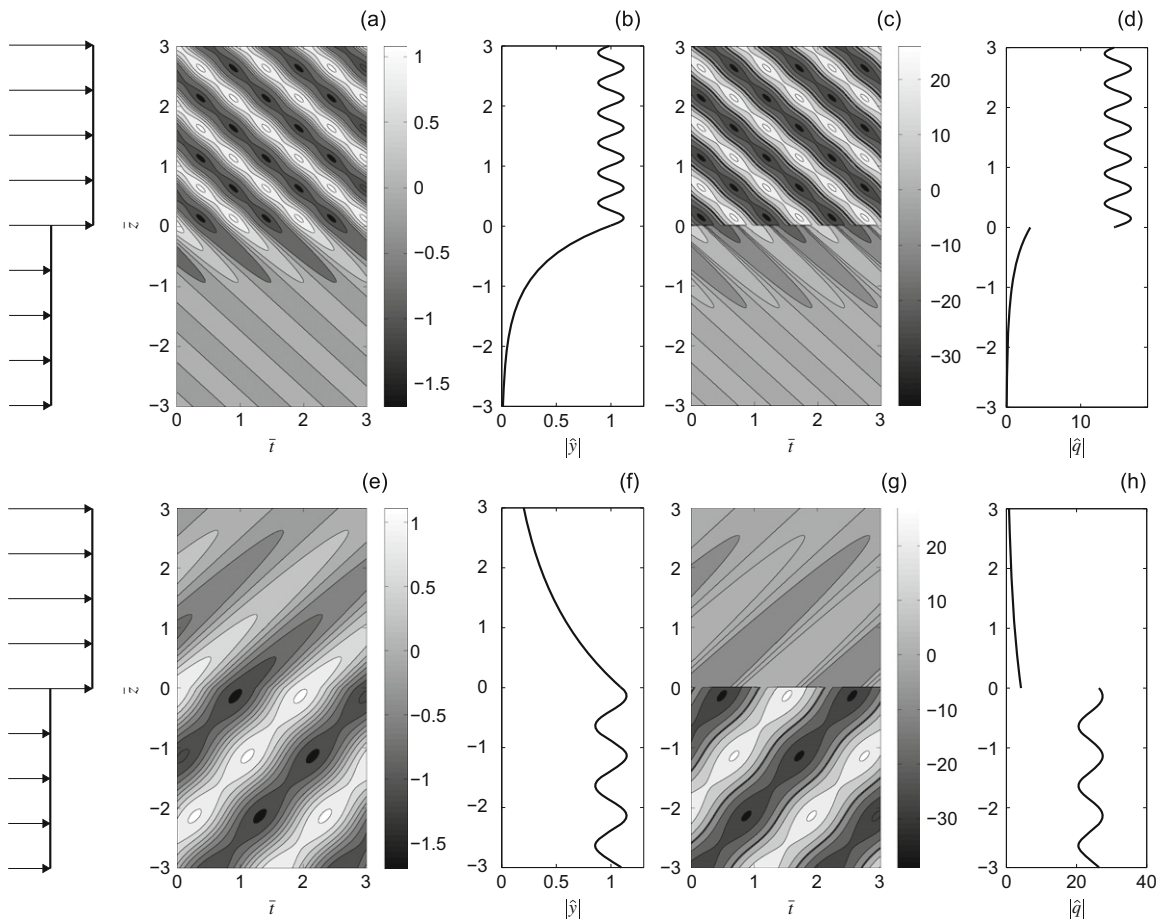
Fig. 9. Unstable cable-wake wave systems for an infinite tensioned cable in non-uniform flows. Top: *primary wave system*, (P). (a) Evolution with time and space of the cable displacement, (b) envelope of the cable displacement, (c) evolution with time and space of the wake, (d) envelope of the wake variable. Bottom: *secondary wave system*, (S). (e) Evolution with time and space of the cable displacement, (f) envelope of cable displacement, (g) evolution with time and space of the wake, (h) envelope of the wake variable. The exponential growth in time of the amplitude omitted for clarity. For all figures, $R = 0.5$ and $AM = 0.25$.

associated with the higher velocity, penetrates into the region of lower velocity. It may therefore be used, in a system of finite length, to estimate the possibility that the secondary wave system persists in the region of lower velocity. A persisting (S) system in the response results in a separation in space of the dominant frequency, a phenomena which we shall refer to here as "space sharing". In Section 5.4, we look into the question of space sharing in a practical case.

5. Comparisons with experimental and numerical results

The linear theory presented in Sections 3 and 4 is now used to analyse some reference cases of vortex-induced vibrations of slender structures published in the literature.

5.1. Range of unstable wavenumbers

In Section 3.1, we have shown that, for a given reduced velocity u, there is a range of real wavenumbers k for which the cable-wake system is unstable in time. Outside of this range of wavenumbers, the waves are neutral so that their amplitude should rapidly be negligible in comparison to their unstable counterparts. We therefore expect wavenumbers of motions observed in practice to fall inside this range.
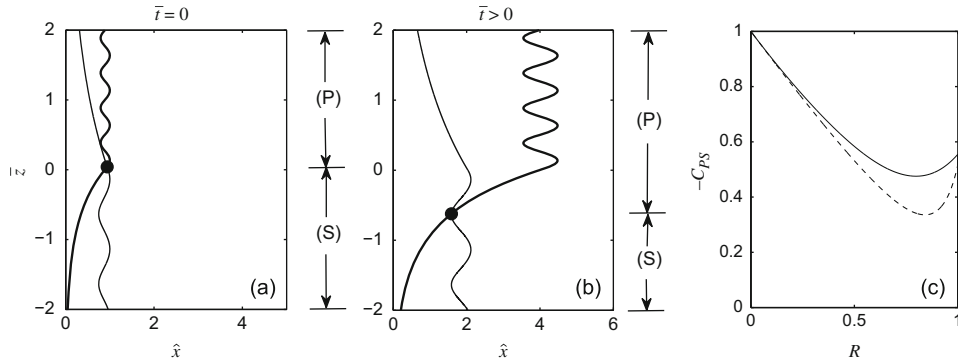
Fig. 10. Schematic view of the competition between the Primary and Secondary wave system. (a), (b) Evolution of the envelopes of each wave system with space and time. Bold line, (P), thin line, (S). The black dot marks the boundary between the two systems, moving with the phase velocity C_{PS}, Eq. (41). (c) Evolution of C_{PS} with the velocity ratio R. $AM = 0.25$ (dashed line) and $AM = 0.8$ (solid line).
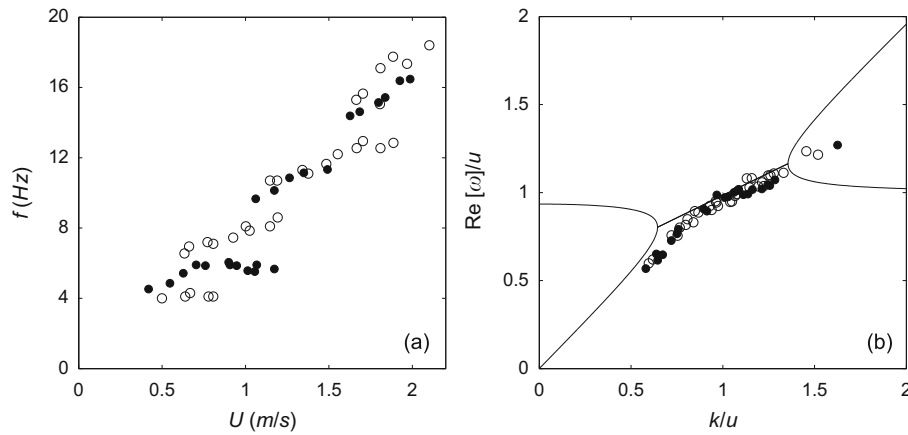

Fig. 11. Comparison between the linear stability analysis and experimental data on the motion of a tensioned cable under uniform cross-flow. (a) Experimental data of the evolution of the vibration frequency f with the flow velocity U, redrawn from King (1995). Results are shown for two different tensions: Θ_1 (black dots), $\Theta_2 = \Theta_1/2$ (open circles). (b) The same data in dimensionless form, compared with the prediction of the linear stability analysis, solid lines.

Table 1
Parameters of experiments and numerical computations.

Parameters	Section 5.1	Section 5.2	Section 5.3	Section 5.4
μ	4.16	π	π	2.785
Γ	–	19.3	34.6	165
L/D	280	469	469	2028
$\partial\theta/\partial z$	–	1.76×10^{-4}	3.16×10^{-4}	–
v	–	–	7.72×10^{-3}	2.79×10^{-3}
Re	9000–40 000	2500–25 000	22 500	1000

To verify this assumption, we use the experimental results by King (1995), who measured the response vibration frequency and mode number of a tensioned cable undergoing VIV in uniform flows. The vibration frequency as a function of the flow velocity is shown in Fig. 11(a), and experimental conditions are summarized in Table 1. The evolution in steps of the frequency with flow velocity mentioned in Section 3.2 for a tensioned cable (Fig. 5) is clearly seen in the experiments.

The experimental results from King (1995) are used here to verify the validity of relations (15) and (16), which give the expected range of unstable wavenumbers and the corresponding frequency of motion. In order to do so, the parameter M from Eq. (7) needs to be quantified. As the mass parameter μ is known, the only inputs needed are C_{L_0} and S_T. For the range of Reynolds numbers considered here, a value of $C_{L_0} = 0.2$ is reported by Norberg (2003). As for the Strouhal number, a value of $S_T = 0.17$ is used, consistent with experimental results from Chaplin et al. (2005b) for similar Reynolds numbers on a tensioned beam under uniform flows. In order to collapse the data onto one graph, the dimensionless frequency $\text{Re}[\omega]$ is normalized by the reduced velocity u. The frequencies and wavenumbers reported by King (1995) are put in dimensionless form using

$$\frac{k}{u} = \left(\frac{n}{2\Lambda S_T}\right)\left(\frac{\Theta}{\frac{\pi}{4}\rho D^2 U(4\mu/\pi - 1)}\right), \quad \frac{\text{Re}[\omega]}{u} = \frac{fD}{S_T U}. \tag{42}$$

The term n refers to the dominant spatial mode observed in the experiment and f to the observed vibration frequency, Fig. 11(a). The comparison between the experimental results and the theoretical prediction, Eqs. (15) and (16), is shown in Fig. 11(b). Most of the experimental points are located inside the range of unstable wavenumbers. Moreover, the normalized frequencies of motion fall very close to the curve predicted by the linear theory.

5.2. Transition between modes

From the analysis presented in Section 3.2 for a finite system, there are possible overlaps of reduced velocity ranges of instability of two (or more) adjacent modes. In the case of such overlaps, we assume that only the most unstable mode is observed in practice. To test this assumption, results from the experimental study of Chaplin et al. (2005b) are used.

A sketch of the experiment is shown in Fig. 12. It consists of a tensioned beam of low flexural rigidity subjected to a uniform water flow on part of its length, the other part being in stagnant water. Chaplin et al. (2005b) represent the transverse displacement of the structure by

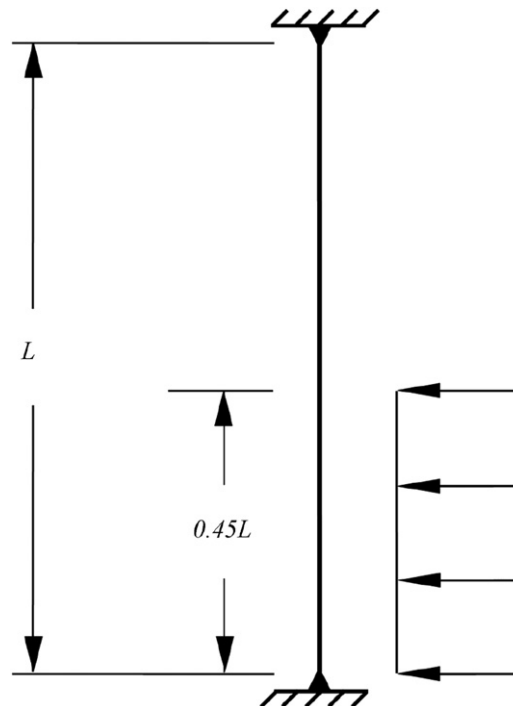$$Y(Z, T) = \sum_n Y_n(T) \sin\left(\frac{n\pi Z}{L}\right), \tag{43}$$

Fig. 12. Schematic view of the experimental setup used by Chaplin et al. (2005b).

where n is the mode number and $Y_n(T)$ is the corresponding modal weight derived from measurements. Note that these modes are not the free vibration modes of the structures. They are now referred to as Fourier modes, to clearly distinguish them from the eigenmodes of the dynamical system.

Fig. 13(a) shows the value of the dominant Fourier mode number for five consecutive flow velocities, as observed in the experiments. In that case Fourier Mode 2 dominates for the low velocities and Fourier Mode 3 for the highest. This transition from Mode 2 to Mode 3 is now analysed using the results of Section 3.2.

In order to properly model this configuration several aspects must be taken into account, which makes it differ from the idealized system described by the set of Eqs. (9) and (10): (a) the beam has a small, but non-negligible bending rigidity, (b) the tension in the beam varies linearly with the vertical position, due to gravity, (c) there is no flow on the upper part of the beam, (d) the damping terms are not neglected. The corresponding set of dimensionless linear equations read

$$\frac{\partial^2 y}{\partial t^2} - \left(\frac{1}{1+\Gamma}\right)\frac{\partial}{\partial z}\left(\theta\frac{\partial y}{\partial z}\right) + \left(\frac{1}{1+1/\Gamma}\right)\frac{\partial^4 y}{\partial z^4} = Mv^2 q - \left(\frac{\gamma}{\mu}v\right)\frac{\partial y}{\partial t}, \tag{44}$$

$$\frac{\partial^2 q}{\partial t^2} - \varepsilon v\frac{\partial q}{\partial t} + v^2 q = A\frac{\partial^2 y}{\partial t^2}. \tag{45}$$

We have used here the dimensionless time variable $t = \mathcal{B}T/D$ defined with the bending wave velocity

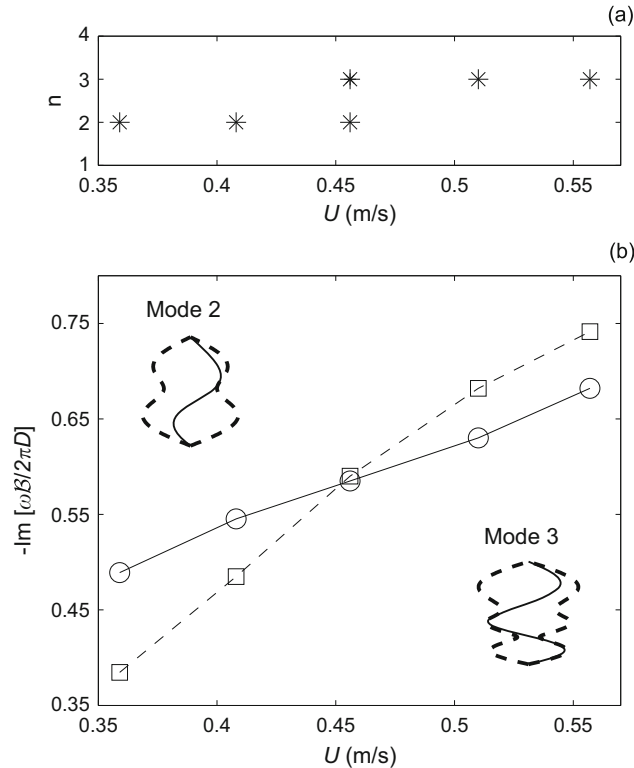$$\mathcal{B} = \sqrt{\frac{\Theta}{m_T} + \frac{EI}{m_T D^2}}, \tag{46}$$

Fig. 13. Mode switching in VIV of a tensioned beam. Comparison between the experimental data and the linear stability theory prediction for the dominant mode: (a) dominant spatial Fourier mode number n in the experiment as reported by Chaplin et al. (2005b), (b) growth rate predicted for Mode 2 (circles) and Mode 3 (squares). Also shown are the computed unstable mode shapes, $|V_y|$ (dashed line) and Re$[V_y]$ (solid line).

recalling here that $m_T = m_S + (\pi/4)\rho D^2 C_{M_0}$. Here $\theta(z)$ is the tension profile equal to one at the top of the structure. The other dimensionless quantities are

$$\Gamma = \frac{EI}{\Theta D^2}, \quad v = 2\pi S_T\left(\frac{U_{\text{ref}}}{\mathcal{B}}\right), \tag{47}$$

where Θ is the tension at the top of the structure, EI is the bending rigidity. The values of the structural parameters are given in Table 1. Note that in the region where no cross-flow exists the fluid force acting on the right-hand side of Eq. (44) is set to zero. In that region the wake variable q is undefined. The flow-induced damping term, scaled by γ, and the wake negative damping term, scaled by ε are those defined in Section 2.1. The structural damping term, proportional to ξ_S, is neglected, being here of much lesser magnitude.

To model the attachments at the structure extremities, conditions of no bending moment and displacement are imposed

$$\frac{\partial^2 y}{\partial z^2}(0, t) = \frac{\partial^2 y}{\partial z^2}(L/D, t) = 0, \quad y(0, t) = y(L/D, t) = 0. \tag{48}$$

As the Reynolds numbers are similar to those of the previous section, the same values of C_{L_0} and S_T are used (King, 1995). A value of $C_D = 2$ is taken for the mean drag coefficient, consistently with measurements of this quantity by Chaplin et al. (2005b).

Eigenmodes of the system defined by Eqs. (44) and (45) with conditions (48) are now computed using a second order centred finite difference scheme in space. The structure displacement is discretized by j points in the spanwise direction and the wake variable by r points only, as no wake model is needed in the upper part of the beam where no flow exists. The discretized form reads

$$[\mathcal{M}]\begin{pmatrix} \ddot{y} \\ \ddot{Q} \end{pmatrix} + [\mathcal{R}]\begin{pmatrix} \dot{y} \\ \dot{Q} \end{pmatrix} + [\mathcal{K}]\begin{pmatrix} y \\ Q \end{pmatrix} = 0, \tag{49}$$

where $\mathcal{Y} = [y_1(T) \quad \cdots \quad y_j(T)]^T$ and $\mathcal{Q} = [q_1(T) \quad \cdots \quad q_r(T)]^T$. The dynamic system (49) is solved for solutions of the form

$$\begin{pmatrix} \mathcal{Y} \\ \mathcal{Q} \end{pmatrix} = \begin{pmatrix} V_y \\ V_q \end{pmatrix} e^{i\omega t}, \tag{50}$$

where ω is the eigenfrequency, and V_y and V_q are the eigenvectors of the structure and the wake respectively. The numerical parameters are chosen to be $j = 300$ and $r = 135$, so that the results become independent of the discretization. Results are now given in terms of dimensional variables, for easier comparison with the experimental results.

The computed growth rates of the two most unstable modes are shown in Fig. 13(b), as a function of the flow velocity parameter. Mode 2 has a growth rate higher than Mode 3 for the lowest velocities. At $U = 0.46$ m/s, the growth rates of both modes are equal and, for higher velocities, Mode 3 becomes the most unstable. This transition in terms of growth rates from Mode 2 to Mode 3 compares well with the experiments where a switch is observed in terms of the dominant mode seen in the response. The corresponding eigenvectors V_y and V_q are complex quantities. Fig. 13(b) shows the structure modal shape V_y for the most unstable mode, respectively Mode 2 and Mode 3 for low and high velocities. These are close to the Fourier mode shapes 2 and 3 assumed in Eq. (43).

It may be concluded that in the present case a simple linear stability analysis can predict some important characteristics of the steady-state response of the system: the most unstable mode corresponds to the observed beam motion.

5.3. Time sharing

In the previous experiments, the response at a flow velocity $U = 0.46$ m/s is a particular case where the time evolution of the modal factors $Y_n(T)$, otherwise strongly periodic, are modulated in time. This type of multimode response is discussed now.

In their paper, Chaplin et al. (2005b) report several cases of what they refer to as "mode switching". The term "time sharing" used by Swithenbank (2007) is also appropriate, and shall be used hereafter to make a clearer distinction from the switch of modes caused by changing the flow velocity, as discussed in the previous section. In the experiments this time sharing was triggered by disturbances such as vibrations in the carriage system due to irregularities in the rails on which it is mounted.

Fig. 14 shows one such case of time sharing in terms of the time evolution of the Fourier modal variables $Y_6(T)$, $Y_7(T)$ and $Y_8(T)$. The flow velocity in this case is $U = 0.90$ m/s. Those time traces are the ones presented in Fig. 7 in
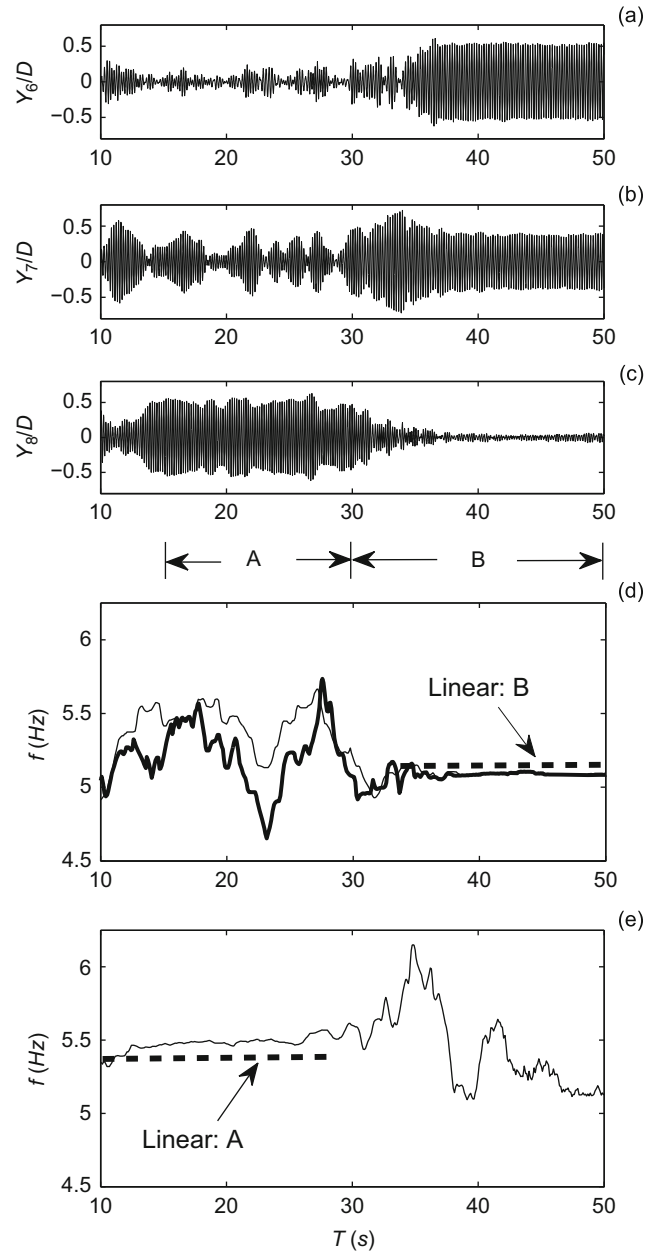
Fig. 14. Time sharing between two regimes of motion in VIV of a tensioned beam, Chaplin et al. (2005b). (a), (c) Time evolution of the modal weight of Fourier Modes 6–8, showing the change of regime, from A to B. (d) pseudo-frequency evolution with time of Mode 7 (thin line) and Mode 6 (thick line), (e) pseudo-frequency evolution with time for modal weight of Mode 8. On (d) and (e), the linear theory prediction for frequencies is shown with dashed lines.

Chaplin et al. (2005b). Two regimes of response are observed. The first regime, named here Regime A, is dominated by Fourier Mode 8 and the second, Regime B, by a combination of Fourier Modes 6 and 7. Fig. 14 also shows the evolution of the pseudo-frequency of the Fourier modal variables $Y_6(T)$, $Y_7(T)$ and $Y_8(T)$ using a wavelet analysis: at each vibration cycle, the frequency corresponding to the maximum wavelet coefficient is noted for each signal, and averaged over 10 cycles of vibrations. For Fourier modes 6 and 7 a constant and common frequency is found during Regime B, when they dominate the response. During Regime A their frequency of motion is ill-defined, as may be expected from the time evolution shown in the upper part of the figure. Conversely, for Fourier Mode 8 a constant
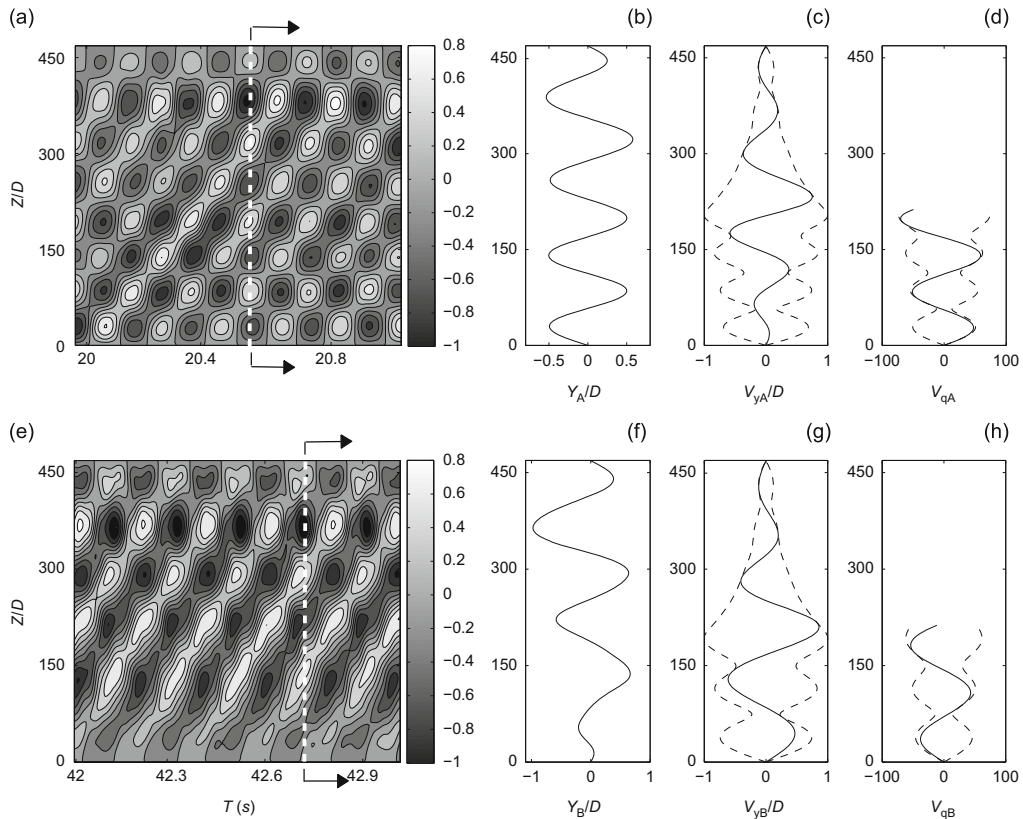
Fig. 15. Characteristics of the two regimes for the case of time sharing, Section 5.3. Experiments by Chaplin et al. (2005b) and most unstable modes using the linear stability theory. Top, Regime A: (a) Experimental evolution with time and space of the structural displacement; (b) a corresponding instantaneous displacement of the structure, at the instant indicated by the arrows in (a); (c) and (d) structure and wake components of one of the two most-unstable modes. Bottom: (e), (h) same information for Regime B and the other most unstable mode.

frequency exists only in Regime A. In Fig. 15 the corresponding experimental space–time evolutions reconstructed using Eq. (43) are shown.

For this configuration, the eigenmode calculation using the coupled linear system (49) predicts that the two most unstable modes have almost identical growth rates, $Im[\omega_A]/Im[\omega_B] = 1.007$. This confirms the possibility of coexistence of these two modes in the response. They can be associated to each regime A or B unambiguously, by considering the dominant wavelength in their spatial evolutions, Fig. 15: one of them is close to a Fourier Mode 8 and the other to a Fourier Mode 6. The eigenfrequencies of these two most unstable modes are shown in Fig. 14, in comparison with the experimental data, showing good agreement.

We may therefore conclude that in the present case time sharing is symptomatic of the fact that two (or more) modes of the linearized system possess similar growth rates and are therefore likely to both exist in the saturated response.

5.4. Non-uniform flow: space sharing

Lucor et al. (2006) reported results of a numerical study on a high aspect ratio tensioned beam free to vibrate only in the cross-flow direction and subjected to non-uniform flows. They solved by direct numerical simulation (DNS) the three-dimensional flow around the structure coupled with the beam dynamics. Two flow profiles were analysed: one linearly sheared called here Case L, and another exponentially sheared called Case E. These are illustrated in Fig. 16. Results for these two cases were found to differ significantly in terms of the dynamics of the beam: in Case L a unique frequency of motion sets on the whole beam, as can be seen on the spatially averaged amplitude spectrum in Fig. 16. Conversely in Case E the beam moves with a local frequency that varies along the span. The spatially averaged
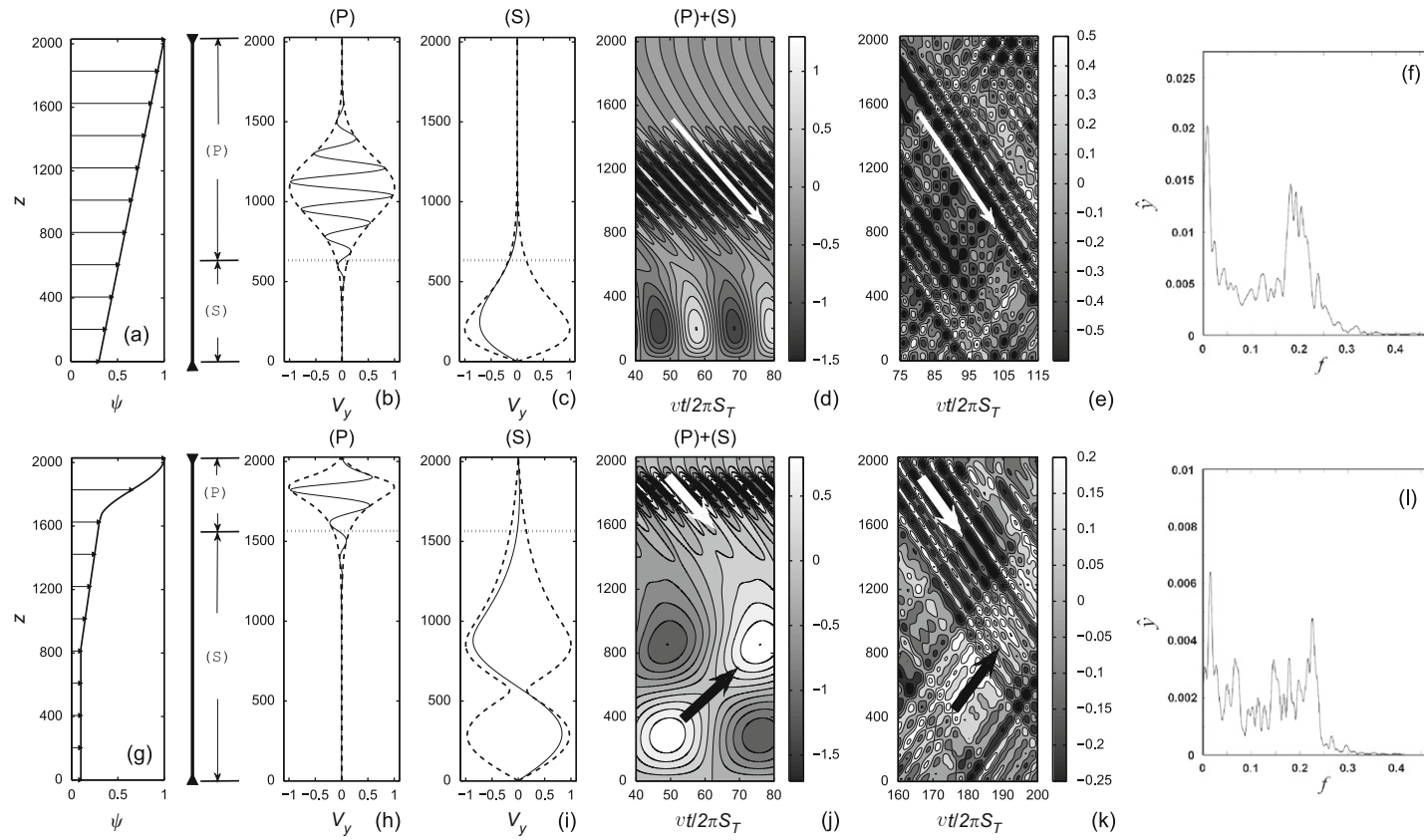
Fig. 16. Tensioned beam undergoing VIV under non-uniform flows. Comparison between numerical predictions by Lucor et al. (2006), using DNS, and the linear stability of the coupled structure-wake system. Top, linearly sheared flow, Case L: (a) flow velocity profile; (b) beam eigenshape for the most unstable mode, Mode (P); (c) same quantity for most unstable mode in the low flow velocity region, Mode (S); (d) reconstructed time space evolution of the beam displacement by recombination of these two modes; (e) time–space evolution in the DNS computation of Lucor et al. (2006); (f) space averaged spectrum of the DNS beam motion. Bottom, exponentially sheared flow, Case E: (g–l) same quantities than above.

Table 2
Linear computation results for Cases L and E.

	$2\pi S_T \omega_P / v$	$2\pi S_T \omega_S / v$	$Im[p_P]$	C_{PS}	L_S	$v t_{PS}/2\pi S_T$
Case L	0.766–0.297i	0.287–0.148i	0.0080	−18.6	660	35.5
Case E	0.827–0.247i	0.117–0.0432i	0.0079	−25.8	1565	60.7

amplitude spectrum shows therefore a large set of frequencies. Lucor et al. (2006) found that the higher frequencies dominate in the upper part of the structure and the lower frequencies in the bottom part. The frequency at the bottom are close to five times lower than the frequencies of the upper part. There is therefore in Case E a clear separation in space of the dominant vibration frequencies that is absent in Case L. These features also appear in the space–time evolution of the displacement of the beam (Fig. 16): for case L a single frequency and a single wavelength combine in a downward propagating wave, but several frequencies and wavelengths coexist in Case E, with a low frequency wave propagating from bottom to top. We seek now to explain these results on the spatial organization of frequencies using the linear theory developed for the case of non-uniform flows in Section 4.

The model used for the beam and the wake dynamics is identical to that of Sections 5.2 and 5.3 except for two aspects: (a) there is no spanwise variation of tension, so that $\theta(z) = 1$, and (b) there is a spanwise variation of velocity so that the dimensionless velocity parameter v must be replaced by $\psi(z)v$ where $\psi(z) = U(Z)/U_{ref}$ is the flow profile. Here the maximum velocity is used as the reference velocity, $U_{ref} = U(L)$. For the drag coefficient C_D and Strouhal number S_T the values of Sections 5.2 and 5.3 are used. We use here a fluctuating lift coefficient of $C_{L_0} = 0.8$ to be consistent with results from Norberg (2003) for the range of Reynolds numbers of Lucor et al. (2006) DNS. The structural parameters can be found in Table 1. The boundary conditions are identical to that of the previous section. Using the same discretization technique as above, the unstable linear modes are derived, in each case of flow profile, L and E. By a simple analogy with the wave systems of Section 4 the modes can be classified as (P) or (S), the former corresponding to the most unstable mode, and the latter being the second most unstable mode localized in the low flow region. The ratios of frequencies and growth rates are given in Table 2. Fig. 16 shows the corresponding eigenvectors. Note that for Mode (P) the eigenvectors are complex, meaning a travelling wave response, while they are essentially real for Mode (S), meaning a stationary response.

In Case L, the maximum amplitude is located in the middle of the domain for (P) and in the lower part for (S). The exponential decay of amplitude with space is clearly seen for both modes. Fig. 16 shows the comparison between the response of the beam in time and space computed by the DNS, and that of the linear model where Mode (P) and Mode (S) are superimposed and the exponential growth in time has been removed. The DNS predicts waves that are propagating downward (indicated by an arrow in the figure), with a velocity that compares well with that of Mode (P). Also, the wavelength of Mode (P) is close to the one obtained by DNS. However, there is no trace of a structural response close to Mode (S) in the DNS prediction. This is precisely the issue of space sharing, which is discussed in the last paragraph of this section.

For Case E, the shape of Mode (P) and Mode (S) are shown in Fig. 16 for the beam displacement. The maximum amplitude region of Mode (P) is then located much higher in the cable than for Case L. Also, Mode (S) has a high amplitude for a much wider zone. Fig. 16 shows the comparison between the DNS calculation and the linear modal analysis results. The superposition of the forms of Mode (P) and Mode (S) is shown. In the upper part of the beam, the linear model predicts well the response computed by Lucor et al. (2006): the wave length and the propagation velocity are well reproduced. As mentioned earlier, one observes in the DNS calculation a low frequency wave in the lower part that propagates upward: in Fig. 16(l), the corresponding low frequency peak is at $f = 0.0158$. This compares reasonably well with the frequency of Mode (S) derived from the result given in Table 2, $f_S = 0.117/2\pi = 0.0186$.

We may conclude that the computed linear Mode (P) provides a good approximation for the wavelength and propagation velocity of the main vibration waves. Three common points with the theory of Section 4 are highlighted. First, a high frequency and dominating mode, with respect to temporal growth rate, Mode (P), has been found for both flow velocity profiles. Second, the wave-length observed for (P) is lower than that of (S). Third, the amplitude of Modes (P) and (S) decreases exponentially outside the range of velocities that is favourable to the establishment of their temporal growth rate. Those common points indicate that the theoretical results in Section 4 for an idealized geometry and flow profile seem applicable to more complex configurations.

Finally, we analyse the issue of the coexistence of several frequencies, or space sharing: as noted above a significant difference between the responses obtained by Lucor et al. (2006) for a linearly sheared flow and an exponentially sheared flow is the coexistence of two zones with distinct frequencies of motion in the latter case. This may be analysed in terms of Modes (P) and (S), using the results of Section 4.4 for an idealized non-uniform flow. The phase velocity of

the invasion of the primary wave system (P) into the region of lower velocity was given by Eq. (41). Here a similar velocity, C_{PS}, may be computed by fitting a spatial decay coefficient on the computed eigenshape of Mode (P), and using the growth rates of the two modes. The time needed for Mode (P) to invade the domain of lower velocities is given by $t_{PS} = -L_S/C_{PS}$ where L_S is the size of the domain of Mode (S), as defined in Fig. 16. Table 2 shows that the invasion time by Mode (P) is longer for exponential shear, case E, than for linear shear, case L. This suggests that Mode (S) is more likely to remain in the actual motion in case E than in case L, and therefore that space-sharing between these two modes is more likely to occur. This is consistent with the results of Lucor et al. (2006), where a more complex frequency content of the response is found in case E.

6. Discussion and conclusions

We have presented here a simple approach to vortex-induced vibrations and waves for slender structures. This simplicity is based on several strong assumptions, which are now recalled. First we have assumed that the local dynamics of lift on the cylindrical section of the structure follows that of a wake oscillator. The concept of wake oscillators has had renewed interest recently, with systematic comparison with experiments and computations that have been made available, and discussion on its physical basis, in particular in relation to global modes. Moreover, it is now more systematically used, as in this paper, without *ad hoc* additional terms that have sometimes been introduced to fit a particular experiment, at the risk of losing generality. Recent applications of this concept of wake oscillators have shown its ability to capture some essential features of VIV, even in complex geometries. Second, we have only considered here the linear stability of a model coupling the structure and the wake dynamics. In doing so we have assumed that the fully saturated state of the system, in its steady-state motion, has characteristics very similar to that of the most unstable linear modes. Third, we have only considered straight cables and beams, assuming that the response for these geometries were somewhat generic. Finally, we have disregarded vortex-induced motion in the direction of flow, which is known to have some effect on the overall response [see for example Jauvtis and Williamson (2004) and Dahl et al. (2007), for the case of a rigid cylinder free to vibrate in both in-flow and cross-flow directions, and Vandiver et al. (2006), for flexible structures].

Because of these assumptions, closed form solutions could be derived for uniform and non-uniform flows. A discretized version of the equations allowed us to use a straightforward eigenmode computation to derive the most unstable modes in more complex cases. Such computation is orders of magnitude faster than a DNS with a flexible cable or beam. Still, the most important result is that several phenomena that have been observed in experiments or computations of VIV of slender structures could be interpreted in this simplified framework: range of unstable wavenumbers, mode transition or mode switching with flow velocity, time sharing and space sharing.

Therefore, the approach presented in the paper may be used for different goals: (a) in a design perspective, as a first step to identify the risk of lock-in and the corresponding frequencies and wavelengths, (b) as a more general tool for the understanding of the complex phenomena observed in VIV of slender structures.

Of course, the linear stability analysis based on wake oscillators has some limitations, many of which can be overcome. First, no estimate of the amplitude of VIV can be obtained. This is not a critical issue, even in practice, as amplitudes in VIV are always close to one diameter or so. Moreover, in terms of fatigue assessment, frequency of motion and wavelength, which affects curvature and therefore stress, are of the utmost importance. These can be derived by the present approach, in the limits where nonlinear effects do not have a significant influence on the local motion and thereby on the local fatigue damage. Second, specific behaviour in time and space that may be caused by nonlinearities of the problem cannot be predicted, for instance hysteretic behaviour of nonlinear coupling between waves. Currently these effects do not seem to play a major role in practical cases of vortex-induced vibrations. Third, the wake oscillator used to model the lift dynamics may be easily improved by considering the dependence of its coefficients with the Reynolds number, or by adding another oscillator for the drag fluctuation. Finally, the adaptation of the present approach to other geometries such as a curved cable would only require a proper linearization of the cable dynamics and a model to take into account the angle between flow and cable axis in the wake oscillator. Similarly, considering a flow that varies in direction along the span requires a proper three-dimensional model of the cable. As of today, a linear stability approach with a wake oscillator is probably the simplest way to explore these cases and understand the complex coupling that arises between the wake and the structure dynamics.

References

Alexander, C., 1981. The complex vibrations and implied drag of a long oceanographic wire in cross-flow. Ocean Engineering 8 (4), 379–406.

Birkoff, G., Zarantanello, E., 1957. Jets, Wakes and Cavities. Academic Press, New York.

Bishop, R., Hassan, A., 1964. Lift and drag forces on circular cylinder in flowing fluid. Proceedings of the Royal Society of London Series A—Mathematical 277 (136), 51–75.

Blevins, R., 1990. Flow-induced Vibration. Van Nostran Reinhold, New York.

Brika, D., Laneville, A., 1993. Vortex-induced vibrations of a long flexible circular-cylinder. Journal of Fluid Mechanics 250, 481–508.

Carberry, J., Sheridan, J., Rockwell, D., 2005. Controlled oscillations of a cylinder: forces and wake modes. Journal of Fluid Mechanics 538, 31–69.

Chaplin, J., Bearman, P., Cheng, Y., Fontaine, E., Graham, J., Herfjord, K., Huarte, F.H., Isherwood, M., Lambrakos, K., Larsen, C., Meneghini, J., Moe, G., Pattenden, R., Triantafyllou, M., Willden, R., 2005a. Blind predictions of laboratory measurements of vortex-induced vibrations of a tension riser. Journal of Fluids and Structures 21 (1), 25–40.

Chaplin, J., Bearman, P., Huarte, F.H., Pattenden, R., 2005b. Laboratory measurements of vortex-induced vibrations of a vertical tension riser in a stepped current. Journal of Fluids and Structures 21 (1), 3–24.

Chomaz, J., 2005. Global instabilities in spatially developing flows: non-normality and nonlinearity. Annual Review of Fluid Mechanics 37, 357–392.

Dahl, J., Hover, F., Triantafyllou, M., Dong, S., Karniadakis, G., 2007. Resonant vibrations of bluff bodies cause multivortex shedding and high frequency forces. Physical Review Letters 99 (14), 144503.

de Langre, E., 2006. Frequency lock-in is caused by coupled-mode flutter. Journal of Fluids and Structures 22 (6–7), 783–791.

Facchinetti, M., de Langre, E., Biolley, F., 2002. Vortex shedding modeling using diffusive van der Pol oscillators. Comptes Rendus-Mécanique 330 (7), 451–456.

Facchinetti, M., de Langre, E., Biolley, F., 2004a. Coupling of structure and wake oscillators in vortex-induced vibrations. Journal of Fluids and Structures 19 (2), 123–140.

Facchinetti, M., de Langre, E., Biolley, F., 2004b. Vortex-induced travelling waves along a cable. European Journal of Mechanics B—Fluids 23 (1), 199–208.

Fujarra, A., Pesce, C., Flemming, F., Williamson, C., 2001. Vortex-induced vibration of a flexible cantilever. Journal of Fluids and Structures 15 (3–4), 651–658.

Gabbai, R., Benaroya, H., 2005. An overview of modeling and experiments of vortex-induced vibration of circular cylinders. Journal of Sound and Vibration 282 (3–5), 575–616.

Gabbai, R., Benaroya, H., 2008. A first-principles derivation procedure for wake-body models in vortex-induced vibration: proof-of-concept. Journal of Sound and Vibration 312 (1–2), 19–38.

Gopalkrishnan, R., 1993. Vortex-induced forces on oscillating bluff cylinders. Ph.D. Thesis, Massachusetts Institute of Technology, Cambridge, MA, USA.

Gosselin, F., de Langre, E., 2009. Destabilising effects of plant flexibility in air and aquatic vegetation canopy flows. European Journal of Mechanics—B/Fluids 28 (2), 271–282.

Griffin, O., Ramberg, S., 1982. Some recent studies of vortex shedding with application to marine tubulars and risers. ASME Journal of Energy Resources Technology 104 (1), 2–13.

Hartlen, K., Currie, I., 1970. Lift-oscillator model of vortex-induced vibrations. Journal of the Engineering Mechanics Division 96 (EM5), 577–591.

Jauvtis, N., Williamson, C., 2004. The effect of two degrees of freedom on vortex-induced vibration at low mass and damping. Journal of Fluid Mechanics 509, 23–62.

Khalak, A., Williamson, C., 1999. Motions, forces and mode transitions in vortex-induced vibrations at low mass-damping. Journal of Fluids and Structures 13 (7–8), 813–851.

Kim, Y., Vandiver, J.K., Holler, R., 1985. Vortex-induced vibration and drag coefficients of long cables subjected to sheared flow. In: Proceedings of the 4th OMAE Symposium, ASME, Dallas, TX, pp. 584–592.

King, R., 1995. An investigation of vortex induced vibrations of sub-sea communications cables. In: Bearman, P.W. (Ed.), Proceedings of the Sixth International Conference on Flow Induced Vibration, London, UK, pp. 443–454.

King, R., Prosser, M., Johns, D., 1973. Vortex excitation of model piles in water. Journal of Sound and Vibration 29 (2), 169–188.

Lie, H., Kaasen, K., 2006. Modal analysis of measurements from a large-scale VIV model test of a riser in linearly sheared flow. Journal of Fluids and Structures 22 (4), 557–575.

Lucor, D., Mukundan, H., Triantafyllou, M., 2006. Riser modal identification in CFD and full-scale experiments. Journal of Fluids and Structures 22 (6–7), 905–917.

Marcollo, H., Chaurasia, H., Vandiver, J.K., 2007. Phenomena observed in VIV of bare risers field tests. In: Proceeding of the 26th International Conference on Offshore Mechanics and Artic Engineering, San Diego, CA, USA.

Mathelin, L., de Langre, E., 2005. Vortex-induced vibrations and waves under shear flow with a wake oscillator model. European Journal of Mechanics B—Fluids 24 (4), 478–490.

Mukundan, H., Modarres-Sadeghi, Y., Dahl, J., Hover, F., Triantafyllou, M., 2009. Monitoring VIV fatigue damage on marine risers. Journal of Fluids and Structures 25, 617–628.

Newman, D., Karniadakis, G., 1997. A direct numerical simulation study of flow past a freely vibrating cable. Journal of Fluid Mechanics 344, 95–136.

Norberg, C., 2003. Fluctuating lift on a circular cylinder: review and new measurements. Journal of Fluids and Structures 17 (1), 57–96.

Py, C., de Langre, E., Moulia, B., 2006. A frequency lock-in mechanism in the interaction between wind and crop canopies. Journal of Fluid Mechanics 568, 425–449.

Sarpkaya, T., 1978. Fluid forces on oscillating cylinders. ASCE Journal of the Waterway Port Coastal and Ocean Division 104 (3), 275–290.

Sarpkaya, T., 2004. A critical review of the intrinsic nature of vortex-induced vibrations. Journal of Fluids and Structures 19 (4), 389–447.

Swithenbank, S., 2007. Dynamics of long flexible cylinders at high-mode number in uniform and sheared flows. Ph.D. Thesis, Massachusetts Institute of Technology, Cambridge, USA.

Trim, A., Braaten, H., Lie, H., Tognarelli, M., 2005. Experimental investigation of vortex-induced vibration of long marine risers. Journal of Fluids and Structures 21 (3), 335–361.

Vandiver, J., 1993. Dimensionless parameters important to the prediction of vortex-induced vibration of long, flexible cylinders in ocean currents. Journal of Fluids and Structures 7 (5), 423–455.

Vandiver, J., 1994. SHEAR 7 program theoretical manual. Massachussets Institute of Technology, Cambridge, MA, USA.

Vandiver, J., Swithenbank, S., Jaiswal, V., Jhingran, V., 2006. Fatigue damage from high mode number vortex-induced vibration. In: Proceedings of the 25th International Conference on Offshore Mechanics and Arctic Engineering. ASME, Hamburg, Germany.

Vikestad, K., Vandiver, J.K., Larsen, C.M., 2000. Added mass and oscillation frequency for a circular cylinder subjected to vortex-induced vibrations and external disturbance. Journal of Fluids and Structures 14 (7), 1071–1088.

Violette, R., 2009. Modèle linéaire des vibrations induites par vortex de structures élancées. Ph.D. Thesis, Ecole Polytechnique, Palaiseau, France.

Violette, R., de Langre, E., Szydlowski, J., 2007. Computation of vortex-induced vibrations of long structures using a wake oscillator model: comparison with DNS and experiments. Computers & Structures 85 (11–14), 1134–1141.

Williamson, C., Govardhan, R., 2004. Vortex-induced vibrations. Annual Review of Fluid Mechanics 36, 413–455.

Xu, W.-H., Zeng, X.-H., Wu, Y.-X., 2008. High aspect ratio (L/D) riser VIV prediction using wake oscillator model. Ocean Engineering 35 (17-18), 1769–1774.